

PCCP

Accepted Manuscript



This is an *Accepted Manuscript*, which has been through the Royal Society of Chemistry peer review process and has been accepted for publication.

Accepted Manuscripts are published online shortly after acceptance, before technical editing, formatting and proof reading. Using this free service, authors can make their results available to the community, in citable form, before we publish the edited article. We will replace this *Accepted Manuscript* with the edited and formatted *Advance Article* as soon as it is available.

You can find more information about *Accepted Manuscripts* in the [Information for Authors](#).

Please note that technical editing may introduce minor changes to the text and/or graphics, which may alter content. The journal's standard [Terms & Conditions](#) and the [Ethical guidelines](#) still apply. In no event shall the Royal Society of Chemistry be held responsible for any errors or omissions in this *Accepted Manuscript* or any consequences arising from the use of any information it contains.

Anisotropy of the n-type charge transport and thermal effects in crystals of a fluoro-alkylated naphthalene diimide: a computational investigation

Cite this: DOI: 10.1039/x0xx00000x

Received 00th January 2012,
Accepted 00th January 2012

DOI: 10.1039/x0xx00000x

www.rsc.org/

Sofia Canola,^a and Fabrizia Negri^{a,b}

The anisotropy of the n-type charge transport of a fluoro-alkylated naphthalene diimide is investigated in the framework of the non-adiabatic hopping mechanism. Charge transfer rate constants are computed within the Marcus-Levich-Jortner formalism including a single effective mode treated quantum-mechanically and are injected in a kinetic Monte Carlo scheme to propagate the charge carrier in the crystal. Charge mobilities are computed at room temperature with and without the influence of an electric field and are shown to compare very well with previous measurements in single-crystal devices which offer a superior substrate for testing molecular models of charge transport. Thermally induced dynamical effects are investigated by means of an integrated computational approach including molecular dynamics simulations coupled to quantum-chemical evaluation of electronic couplings. It is shown that charge transport occurs mainly in the *b,c* crystallographic plane with a major component along the *c* axis which implies an anisotropy factor in very good agreement with the observed value.

Introduction

Naphthalene diimide (NDI) derivatives are promising n-channel organic semiconductors^{1–3} due to their easy synthesis from commercially available precursors combined with their high electron affinity and the tenability of their optoelectronic properties. Core-substituted NDIs are emerging as a class of conducting and functional materials.^{4–6} As for perylene diimide (PDI) derivatives,^{7,8} chemical substitution at the imide nitrogens influences molecular packing in the solid state and therefore their charge transport properties and mobility.^{9,10} NDI derivatives without core substitution have shown remarkable high field effect mobilities ($6 \text{ cm}^2/\text{Vs}$ ¹¹) although suffering by lack of stability under ambient conditions. Ambient stability can be improved by introducing strongly electron-withdrawing groups such as fluoroalkyl groups.^{12–14} Fluoro-alkylated and non-fluorinated analogues were synthesized and used to fabricate solution cast n-channel field effect transistors (FETs). Recently core-chlorinated NDI derivatives with different fluorinated side chains^{13,14} have shown electron mobilities up to $1.43 \text{ cm}^2/\text{Vs}$ in thin film transistors prepared by vacuum deposition or solution shearing deposition. More recently, remarkably high mobilities up to $8.6 \text{ cm}^2/\text{Vs}$ have been measured on ribbon-shaped crystals¹² of one of the three core-chlorinated NDI derivatives previously studied in thin films. Computational investigations on electron transport in NDI derivatives have been reported¹⁵ and have shown an interplay between intermolecular interactions and molecular packing.

A single crystal of a pi-conjugated molecule represents a superior substrate for the study of its electric properties since the trap density originating from structural defects and hopping barriers among grains are minimized. This enables the evaluation of charge carrier mobilities close to the intrinsic values of the molecular material that can be compared with those determined by appropriate modelling. Recently, the n-type charge transport of the fluoro-alkylated NDI derivative shown in Figure 1, previously investigated in thin film transistors,⁹ has been investigated in single-crystal devices fabricated with the ‘organic ribbon mask’ technique.^{16,17} The two dimensional hexagonal shape of the crystals grown allowed the measurement of charge transport anisotropy which resulted in a factor of 1.6. The highest mobility of $0.7 \text{ cm}^2/\text{Vs}$ was measured along the *c* axis, while mobility along the *b* axis did not exceed $0.45 \text{ cm}^2/\text{Vs}$.¹⁶

We have recently investigated the combined effect of intra- and inter- molecular properties on the charge transport of some fluorinated and chlorinated PDI derivatives^{18,19} with an integrated approach involving quantum-mechanical (QM) calculations, classical molecular dynamics (MD) and kinetic Monte Carlo (KMC) simulations. In previous investigations we showed that for core unsubstituted PBI derivatives¹⁹ thermally induced disorder effects^{18–24} modulate remarkably the intracolumn electronic coupling, thereby contributing to the measured electron mobility while a *retardation effect* depresses mobility for crystals containing both enantiomers of core-twisted PDIs.

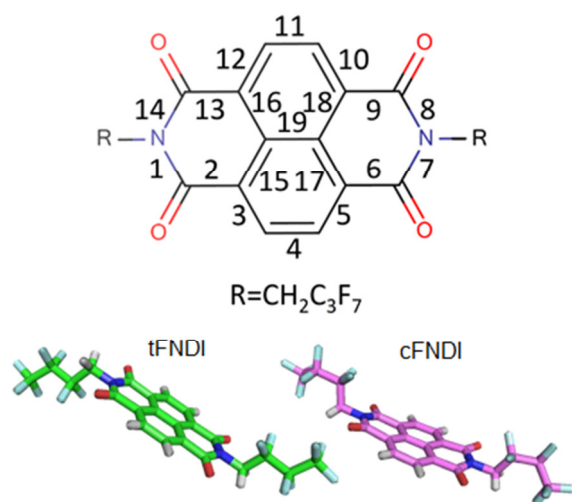


Figure 1. (top) Structural formula of the NDI derivative considered in this work and (bottom) the two conformers **tFNDI** and **cFNDI** that form the crystal.

Prompted by the availability of measurements in single crystals,¹⁶ here we investigate the charge transport properties of the fluoro-alkyl NDI derivative of Figure 1, hereafter labelled **FNDI**. Because the crystal of **FNDI** includes two conformers, one in which the imide fluoroalkyl substituents are on the opposite side with respect to the molecular plane (substituents in *trans* hereafter labelled **tFNDI**) and one in which the imide substituents are on the same side with respect to the molecular plane (substituents in *cis* hereafter labelled **cFNDI**), as shown in the bottom part of Figure 1, both were considered in the calculations. The aim is to explore the effect of intra-molecular and inter-molecular parameters paying also attention to the possible role of thermally induced dynamical effects. To this end we employed the previously introduced multi-scale protocol: QM methods were employed to evaluate of inter and intra-molecular charge transport parameters required to estimate charge transfer rate constants. These were injected in a KMC scheme for the propagation of the charge carriers in the crystals with and without the effect of an electric field, to provide estimates of charge mobility and its anisotropic character. Finally, based on the previously reported strong effects of thermally induced dynamical disorder for PDI derivatives, MD simulations, combined with QM evaluation of electronic couplings, were employed to investigate the extent of fluctuations and the inter-molecular motions responsible for them.

Modeling electron transport

Equilibrium structures of neutral and charged species were obtained without imposing symmetry from quantum-chemical calculations carried out at B3LYP/6-31+G* level of theory. Beside **FNDI** also a model system featuring hydrogen atoms at the core and imide positions, hereafter labelled **HNDI**, was considered for comparison. The nature of the stationary points determined by quantum-chemical structure optimizations was assessed by evaluating vibrational frequencies at the optimized geometries. Vibrational frequencies were also employed to estimate the vibrational contributions to the intra-molecular

reorganization energies through the calculation of Huang-Rhys parameters^{25,26} (see the Supporting Information section).

Vertical electron affinities (VEA) of NDI derivatives were directly estimated as energy differences between neutral and charged species both computed at the geometries optimized for the neutral (VEAn) or the charged (VEAc) species (see also Figure S1). All the quantum-chemical calculations were carried out with the Gaussian09 suite of programs.²⁷

Bulk charge transport was investigated according to the hopping mechanism^{21,25,26} and charge mobilities were evaluated a) assuming a Brownian motion of the charge carrier,²⁸ that is in the limit of zero field and zero concentration and b) under the effect of an electric field.

The validity of the non-adiabatic hopping model depends on the relative magnitude of the charge transfer integral V_{ij} and the reorganization energy parameter λ , with V_{ij} required to be considerably smaller than λ .^{21,29} As it will be shown, we are within this limit for the molecule investigated here. In this scheme the relevant charge transfer event is localized on a molecular pair (dimer) formed by two neighbouring molecules. The organic semiconductor material was studied in the crystalline form used in the experimental investigation¹⁶ and the possible dimers were identified by evaluating the distances between the centres of mass of the molecules surrounding a central reference molecule in the crystal.

Although several computational investigations have previously employed the simpler Marcus formulation for charge transfer rate constants, we note that, because the quantum nature of the most active modes governing local electron-phonon coupling cannot be neglected, a more suitable formulation of the transfer rate constants k_{eT} associated with each hopping event is provided by the Marcus-Levich-Jortner (MLJ) quantum correction^{30,31} of the Marcus equation.³² The MLJ expression can be derived, similarly to the rate constant for energy transfer,³³ from Fermi's Golden rule,³¹ and reads:

$$k_{eT} = \frac{2\pi}{\hbar} V_{ij}^2 \frac{1}{\sqrt{4\pi\lambda_{class}k_B T}} \sum_{v=0}^{\infty} \exp(-S_{eff}^v) \frac{S_{eff}^v}{v!} \times \exp\left(-\frac{(\Delta G^0 + \lambda_{class} + v\hbar\omega_{eff})^2}{4\lambda_{class}k_B T}\right) \quad (1)$$

In the expression above, beside the electronic coupling V_{ij} (or charge transfer integral, see the Supporting Information section for details), λ_{class} is the classical contribution to the reorganization energy and ΔG^0 is the free energy associated with the self-exchange processes considered in this work ($M^0 + M^c \rightleftharpoons M^c + M^0$, M^0 being the organic species in the neutral state, M^c being the organic species in its charged state). Energetic disorder^{26,34} was neglected and it should be noted that in the one-electron approximation adopted to model electronic couplings, the site energy difference between **tFNDI** and **cFNDI** molecules is zero (see the LUMO energies in Table 1) and therefore ΔG^0 was set equal to $-e \cdot \vec{F} \cdot \vec{d}$, where \vec{F} is the vector associated with the electric field and \vec{d} is the vector connecting the two molecular sites forming the dimer. Equation (1) includes the quantum description of the non-classical degrees of freedom represented by a single effective mode of frequency ω_{eff} and associated Huang-Rhys (HR) factor S_{eff} . Because the low frequency vibrations can be described, to a

good approximation, in classical terms, and because of their possible anharmonicity, the contributions for frequencies below 250 cm^{-1} were not included in the evaluation of ω_{eff} . The exceeding classical contributions were summed to the outer sphere reorganization energy and included in the λ_{class} parameter of the MLJ equation (1). The outer sphere contribution to the reorganization energy was assumed to be 0.001 eV , in keeping with recent studies.³⁵

The calculation of the Brownian mobilities was performed by considering the three dimensional crystal structures¹⁶ of the investigated systems, and by computing the diffusion coefficient D with a set of kinetic Monte Carlo (KMC) simulations³⁶⁻⁴⁴. In each KMC simulation a single charge carrier was let move on the crystal via hopping events occurring between near neighbours molecules forming a dimer. The probability P_n associated with the hopping event that moves the charge carrier to the n neighbour of a given molecule was determined by the MLJ charge transfer rate constant k_n as $P_n = (k_n / \sum_j k_j)$, where j runs over possible paths for a charge localized on a given molecular unit in the crystal. The time associated with the electron transfer to the n th neighbour is $-\ln(X)/K_{\text{tot}}$ where X is a random number uniformly distributed between 0 and 1 and $K_{\text{tot}} = (\sum_j k_j)$. The distance associated with the hopping is that between the centres of mass of the two molecules forming the dimer. The trajectory is propagated by selecting randomly one molecule in the crystal as the starting point. A list of possible neighbours is available and the trajectory is advanced by choosing a random number r uniformly distributed between 0 and 1 and by selecting the j th neighbour such that $\sum_n^{j-1} P_n < r \leq \sum_n^j P_n$. The position of the charge carrier was saved and accumulated for groups of 2000 trajectories. An approximately linear dependence^{42,45} of the mean square displacement (MSD) $\langle [r(t) - r(0)]^2 \rangle$ as a function of time t was obtained by averaging over subsets of 2000 KMC trajectories. The diffusion coefficient D was readily obtained from the fitted linear dependence of the MSD employing the Einstein equation: $D = \lim_{t \rightarrow \infty} (\text{MSD}/6t)$.

Ten subgroups of 2000 trajectories each, were produced and the final charge mobilities were obtained by averaging over those computed for each subgroup. Each KMC trajectory consisted of typically of 10^6 moves and the temperature T was set to 300 K . Charge mobilities were obtained from D with the Einstein-Smoluchowski equation:

$$\mu = \frac{eD}{k_B T} \quad (2)$$

The components of the diffusion tensor (and of the mobility tensor) were evaluated according to

$$\mu_{\alpha,\beta} = \frac{D_{\alpha,\beta}}{k_B T} = \lim_{t \rightarrow \infty} \frac{(\Delta r_\alpha \Delta r_\beta)}{6tk_B T} \quad (3)$$

where Δr is the charge displacement at time t and $D_{\alpha,\beta}$ is the diffusion tensor, where $\alpha, \beta = x, y, z$.

For comparison, the diffusion coefficient was also estimated according to the more approximate isotropic formulation:

$$D = \frac{1}{2d} \sum_n (r_n)^2 k_n P_n \quad (4)$$

Here n runs over possible hopping events for a charge localized on a given molecular unit in the crystal, d is the dimensionality of the system, r_n is the distance between the centre of mass of the starting molecule and the neighbouring molecule in the hopping event.

In the presence of electric field, time of flight (TOF) charge mobilities were obtained as^{37,46,47}

$$\mu = \frac{d_f}{\tau F} \quad (5)$$

where F is the magnitude of the electric field (10^5 V/cm), d_f is the distance travelled by the charge along the F direction and τ is the time required to travel the distance d_f . The latter was taken of the order of the channel length used to fabricate the devices, namely about $5\text{-}50\text{ }\mu\text{m}$ and the mobility was averaged over 100 trajectories.

To assess the importance of thermal motions to modulate the electronic couplings, we run MD simulations, combined with the QM evaluation of charge transfer integrals, for **FNDI**.

Molecular dynamics simulations were run on a supercell $3 \times 3 \times 3$ of the crystal unit cell of **FNDI**. The dynamics of the system was studied with periodic boundary conditions employing the MM3 force field⁴⁸ and the Tinker code.⁴⁹ Since recent studies have shown that low frequency intermolecular vibrations can modulate the magnitude of the electronic couplings, we froze all the intra-molecular degrees of freedom and kept the molecule in the cell, rigid at its crystal structure, while allowing inter-molecular motions. We run a 100 ps MD simulation in the NVT ensemble and at $T = 300\text{ K}$, using the Berendsen's algorithm⁵⁰ to simulate the presence of a thermal bath. The integration time step was set to 1 fs . The transfer integrals between LUMO orbitals were evaluated every 30 fs for the most relevant molecular dimers of **FNDI**.

Results and Discussion

Intra-molecular properties

From the equilibrium structures of neutral and charged species of both **tFNDI** and **cFNDI** we estimated both electron affinities and intramolecular reorganization energies (see Figure S1). Fluorine substitution at the imide positions lowers the energy of the LUMO level (see Figure S2 for a graphical representation of frontier orbitals) and increases the electronic affinity, thereby strengthening the n-type character of the semiconductor. This effect can be appreciated by comparing the energies of the LUMO levels of **tFNDI** and **cFNDI** reported in Table 1 and the correspondingly computed vertical and adiabatic EAs in Table S2 with those of the model compound **HNDI**. The computed LUMO energies of these NDI derivatives are in good agreement with those estimated from experimental reduction potentials.¹⁴

The intramolecular reorganization energies of **FNDI** (collected in Tables S2, S3) estimated from the adiabatic potential method,^{25,26} fall in the region 0.38 eV and are very close to those determined from the Huang-Rhys factors. These computed values are relatively large compared with those of

bay unsubstituted PDI derivatives (of the order of 0.26 eV), and in line with those of other NDI derivatives.¹⁵ The computed vibrational contributions to the intramolecular reorganization energies are collected in Figure S3 and Tables S4-S5 from which it is seen that the active modes are very similar for neutral and anionic states. The contributions from frequencies above 250 cm⁻¹, namely the frequencies that cannot be considered classical, were employed to estimate the effective parameters of the single quantum mode in eq(1). The remaining contributions were included into the λ_{class} parameter.^{18,19,51} together with the outer-sphere term (see Table 2). These parameters were employed to estimate the charge transfer rate constants according to eq. (1). Owing to the small difference between the intra-molecular parameters of **tFNDI** and **cFNDI**, a common set obtained as the average of the two, was used to evaluate rate constants for the KMC simulations.

Figure S4 collects the computed bond lengths (neutral and anionic species) of the two **FNDI** derivatives. A summary of geometry changes upon doping is depicted in Figure 2, from which it can be seen that the geometry change is almost identical for the **tFNDI** and **cFNDI**. The largest bond length variations occur for the peripheral bonds 2, 4, 6, 9, 11 and 13, whose length decreases upon doping and for bond 3, 5, 10 and 12, whose length increases upon doping, while the CC bonds internal to the conjugated chromophore display modest changes with the exception of the central bond 19. The charge transfer will be assisted by vibrational modes displaying a not negligible projection over this geometry change, as confirmed by the inspection of modes exhibiting the largest contributions to the reorganization energy and depicted in Figure S5.

Table 1 Frontier orbital energies of **tFNDI**, **cFNDI** and model compound **HNDI** computed at the B3LYP/6-31+G* optimized structures of the neutral species along with the transport gaps computed at the optimized structures of the neutral and anionic species.

B3LYP/6-31+G*	$E(HOMO) / eV$	$E(LUMO) / eV$	$\Delta E_{geo-neutral}$	$\Delta E_{geo-anion}$
tFNDI	-7.73	-4.15	3.57	3.24
cFNDI	-7.72	-4.15	3.57	3.24
HNDI	-7.51	-3.93	3.59	3.25

Table 2 Effective frequency ω_{eff} and associated Huang-Rhys factor S_{eff} employed in the evaluation of charge transfer rate constants of the NDI derivatives investigated in this work.

B3LYP/6-31+G*	tFNDI	cFNDI	KMC ^d
ω_{eff} / cm^{-1} ^a	975	967	971
S_{eff} ^a	3.058	3.152	3.105
λ_i / eV ^b	0.370	0.378	0.374
Intra-molecular λ_{class} ^c	0.012	0.010	0.011
Total λ_{class}	0.013	0.011	0.012

^a Only frequencies above 250 cm⁻¹ were considered in the calculation of the effective parameters. A value of λ_e of 0.001 eV was assumed based on recent estimates.³⁵ ^b Computed from the adiabatic potential method. ^c Contribution from intra-molecular classical vibrations. ^d Average of the parameters computed for the two conformers employed in the KMC simulations.

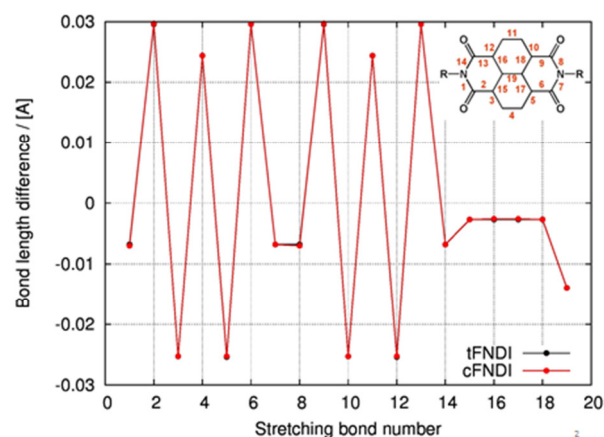


Figure 2. Computed bond length changes upon charging (neutral-anion) for **tFNDI** (black) and **cFNDI** (red) (B3LYP/6-31+G*). Bond numbering as depicted in the inset.

Charge transport and anisotropy

The crystal of **FNDI** belongs to the monoclinic $P/2c$ group.¹⁶ The **FNDI** molecules assemble in well separated planes along the a axis and, within a plane laying parallel to the b,c crystallographic plane, alternating rows of **tFNDI** and **cFNDI** molecules assemble to form a layer (see Figure S6). Accordingly, the charge transport is discussed in terms of *intra-layer* and *inter-layer* jumps for **FNDI**. To investigate the possible charge hopping paths we extracted, from a portion of the crystal, all the possible neighbors of a given molecule. The distribution of distances between centers of mass at the crystal structure (along with the radial distribution function extracted from the MD simulations that will be discussed in the next section) are collected in Figure S7. The Figure shows that there are a number of charge jumps associated with distances lower than 10 Å. The most important paths for charge-propagation, depicted in Figure 3, were selected on the basis of their computed electronic couplings V_{ij} collected in Table 3. Only charge jumps associated with not negligible electronic couplings were included in the KMC simulations. Inspection of Table 3 shows that the only active channels for charge propagation are *intra-layer*. Indeed we could not find significant electronic couplings for *inter-layer* paths, some of which (those displaying the shortest distances between monomers) are depicted in Figure S8. The most efficient *intra-layer* paths, shown by arrows in Figure 3, correspond to jumps from **tFNDI** to **cFNDI** molecules (paths D1 and D2) or between molecules of the same type (paths D4 and D5). The two *intra-layer* jumps D1 and D2 originate from the presence

of two different reciprocal orientations of **cFNDI** and **tFNDI** molecular sites in the crystal. Molecular orientation governs the magnitude of the corresponding electronic coupling which is indeed larger for path D2 compared to D1, owing to a better overlap between conjugated cores of the two interacting chromophores. Path D4 and D5 are associated with very similar distances between the centers of mass which are, however, considerably larger than those of paths D1 and D2. This explains their reduced magnitude compared with the couplings associated with paths D1 and D2. In between these two pairs of charge hops there is another path labelled D3t and D3c (see Figure 3) which is associated with a distance between centers of mass smaller than that of paths D4 and D5. Nevertheless the coupling is computed to be negligible (1 cm^{-1}) because in this case the center of mass distance coincides with the separation between molecular planes which is much larger than for dimers D4 or D5. In the latter case a better overlap is reached for dimer D5 between **cFNDI** molecules than for dimer D4 between **tFNDI** conformers.

The couplings discussed above were used to generate, together with the intra-molecular parameters, the set of rate constants (see Table 3) required by the KMC simulations. When the electric field is applied, backward and forward rate constants for the same dimer can differ, as shown in the Table. We note that the hopping approach is justified here since the largest coupling (522 cm^{-1}) is considerably smaller than the polaron binding energy ($1/2\lambda_i$) which is about 1540 cm^{-1} .²¹

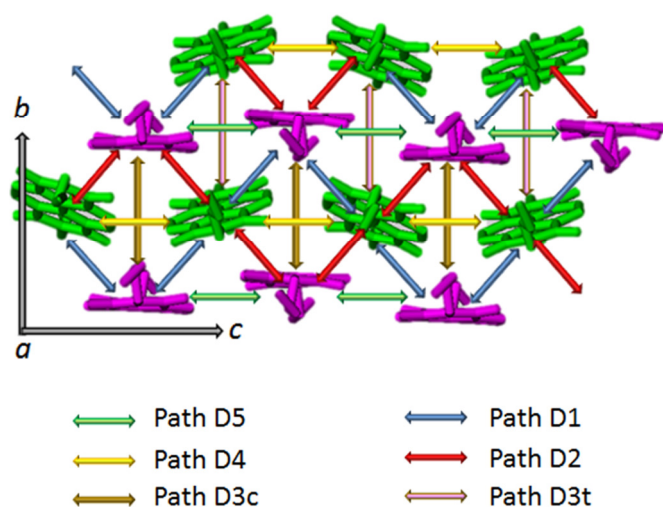


Figure 3. Intra-layer charge paths for the crystal of **FNDI**. Green molecules are **tFNDI**s while purple molecules are **cFNDI**s. Fluorine and hydrogen atoms not shown for clarity.

Table 3 Electronic couplings V_{ij} (B3LYP/6-31G* level of theory) and charge transfer rate constants k_{CT} computed for the different charge hopping paths in the crystal of **FNDI**.

dimer	Intra-layer distance (Å)	V_{ij}^{LUMO} (cm^{-1})	k_{CT}^{a} (ps^{-1})	k_{CT}^{b} (ps^{-1})	k_{CT}^{c} (ps^{-1})
tFNDI					
D1	5.6568	522	25.78	23.67-27.43	27.56-23.45
D2	5.7460	346	11.28	10.32-12.03	10.26-12.06
D3t	7.7605	1	/	/	/
D4	8.3540	175	2.953	2.953-2.953	3.282-2.375
cFNDI					
D1	5.6568	522	25.78	27.43-23.67	23.45-27.56
D2	5.7460	346	11.28	10.32-12.03	10.26-12.06
D3c	7.7605	1	/	/	/
D5	8.3550	199	3.814	3.804-3.824	3.067-4.238

^a Without applied electric field. ^b Electric field applied along *b*. ^c Electric field applied along *c*.

As a result of the above pattern of possible charge jumps, the KMC charge propagation in crystals of **FNDI** occurs in the crystallographic *b,c* plane with a more marked tendency along the crystallographic *c* direction (see Figure 4 where a number of KMC trajectories are displayed). The preferential motion along the *c* direction is due to the fact that, as seen in Figure 3, the yellow (D4) and green (D5) pathways follow the *c* direction. In addition the red (D2) and blue (D1) most efficient channels follow a zig-zag pathway also along the *c* direction. In contrast, along the *b* direction the charge carrier must follow a sequence of alternating red and blue pathways, having different efficiencies and therefore giving rise to a mechanism of dimer trapping similar to that occurring in core-twisted chlorinated PDI derivatives.^{18,19} This mechanism is expected to depress the charge mobility, as evidenced by inspecting a short portion of a KMC trajectory in Figure S9, showing the propagation of the charge along the *b* direction as a function of time, in which several traces of the dimer trapping effect (namely several sequential oscillations back and forth inside the same dimer) can be seen.

The computed Brownian mobility, according to eq. (2), is $1.77 \text{ cm}^2/\text{Vs}$. Note that this value is substantially different from the value [$0.42 \text{ cm}^2/\text{Vs}$] obtained from the more approximate isotropic formulation where the diffusion coefficient is estimated using eq. (4).⁵² From the diagonalization of the mobility tensor (see Table S6) the largest eigenvalue is associated with the *c* direction and the second largest with the *b* directions (see Table 4), in agreement with the above discussion pointing to a more efficient transport along *c*.

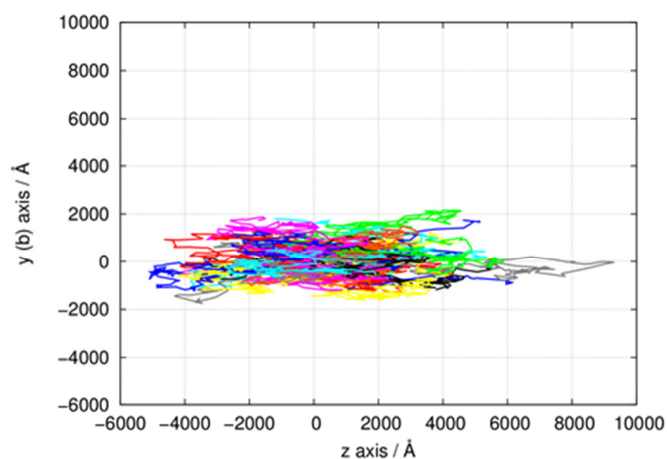


Figure 4. Plot of a number of trajectories, each trajectory with a different colour, in the $y(=b),z$ plane from KMC simulations without applied electric field, showing the 2D charge transport character with a dominant contribution along z . Note that the c crystallographic direction is principally along z .

An additional approach to investigate anisotropy is based on the application of an electric field in various directions followed by the calculation of the corresponding charge mobility.⁵³ Application of an electric field along the *intra-layer* directions b and c increases both computed mobilities by a factor of three (see Table 4) but does not change the magnitude of the anisotropy ratio (1.8) which is equal to that computed in the absence of electric field and also very close to the observed value (1.6). A complete study of the anisotropy was carried out in the b,c , the a,b , the b,z and the a,z planes, by rotating the direction of the field in steps of 15 degrees. A graphical summary is shown in Figure 5. Finally we note that the computed mobilities are of the same order of magnitude of the observed ones. Although the model contains a number of approximations that may account for discrepancies, we note that, often, observed values smaller than computed ones, may be ascribed to the presence of impurities in the crystals compared with the ideal perfect nature of the simulated crystals.

Table 4 Computed electron mobilities μ for the crystals of FNDI and comparison with experimental data.

compound	$\mu^a / \text{cm}^2\text{V}^{-1}\text{s}^{-1}$	$\mu^b / \text{cm}^2\text{V}^{-1}\text{s}^{-1}$	$\mu_{\text{exp}} / \text{cm}^2\text{V}^{-1}\text{s}^{-1}$
FNDI	1.77		
	0.63 (b axis) ^c 1.14 (c axis) ^c	1.87 (b axis) 3.34 (c axis)	0.45 (b axis) ^d 0.70 (c axis) ^d
Anisotropy c/b	1.8	1.8	1.6 ^d

^acharge mobility in the absence of applied electric fields. ^bcharge mobility for an electric field of 10^5 V/cm directed as indicated in parenthesis. ^cThe two largest eigenvalues and eigenvectors (in parenthesis) of the mobility tensor. ^dFrom ref.¹⁶

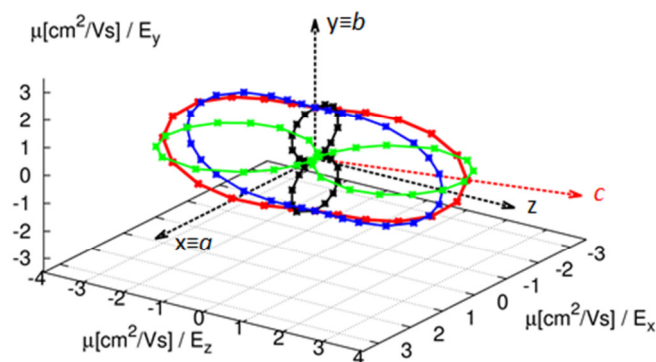


Figure 5. Charge transport anisotropy for the crystal of FNDI. Anisotropy in the b,c crystallographic plane (red); anisotropy in the $y(=b),z$ plane (blue); anisotropy in the $y(=b),x(=a)$ plane (black); anisotropy in the $x(=a),z$ plane (green)

Non-local electron-phonon interactions and their intermolecular representation

To assess the role of thermally induced dynamical effects, namely the electronic coupling fluctuations related to the magnitude of non-local electron-phonon couplings, we carried out an analysis along the lines of our previous work.¹⁸⁻²⁰ Because electron-phonon coupling is mediated by intermolecular vibrations whose frequency values are generally below 200 cm^{-1} , those effects can be suitably determined based on an integrated classical MD/QM approach.²¹ The fluctuations were computed for the four electronic couplings D1, D2, D4 and D5. Figures 6 and S10 collect the distribution of electronic couplings as a function of time and their fitting with a Gaussian function. The strength of the non-local electron-phonon coupling can be evaluated by the thermal fluctuation of the transfer integral⁵⁴ and more precisely by evaluating the standard deviation σ

$$\sigma^2 = \left\langle \left(V_{i,j} - \langle V_{i,j} \rangle \right)^2 \right\rangle \quad (6)$$

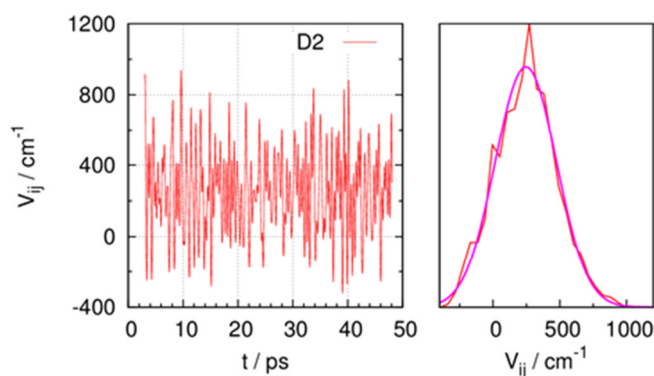


Figure 6. Thermally induced disorder effects (300K) on the distribution of the electronic coupling associated with the D2 pathway. (left) Fluctuation of the computed electronic couplings as a function of time; (right) Gaussian fitting (magenta) of the dispersion of computed couplings (red).

The D4 and D5 couplings show modest standard deviations ($\sigma=28$ and 68 cm^{-1} , respectively, see Table S7), while the σ of the D1 coupling (111 cm^{-1}) is considerably larger and that of the D2 coupling (230 cm^{-1}) is close to the size of the coupling itself, ca. 350 cm^{-1} .

Note that, from the computed radial distribution function (see Figure S7) the extent of inter-molecular displacements is similar for all the dimers of **FNDI** investigated. Therefore, the reduced electronic coupling fluctuations for dimers D4 and D5 compared to those of dimers D1 and D2, must be ascribed to a reduced efficiency of π -stacking and orbital overlap rather than to reduced intermolecular motions.

Inspection of Figure 7 shows that while for couplings D1, D4 and D5 a good correlation is found between the center of mass (CoM) distance variation and the modulation of electronic couplings, this is not equally clear for coupling D2. This suggests that not only the distance but also molecular reorientation plays a role in the modulation of D2 electronic couplings.

A suitable way to monitor molecular orientation when intra-molecular degrees of freedom are frozen, as in this case, is to evaluate Euler angles. The Euler angles are three angles that describe the orientation of a rigid body and represent a sequence of three elemental rotations. In the specific case, these rotations start from the principal inertial axes centered on each molecule and lead to the final coordinate system corresponding to the orientation of the molecules in the crystal.¹⁶ Angles ϕ , θ and ψ correspond to rotations around Z, Y and X principal axes, respectively. Since the orientation of each molecule can change during the dynamics, the fluctuations of Euler angles provide a measure of molecular reorientation. To gain further insight on the molecular motions that favor non-local electron-phonon couplings, we examined the Euler angles for each snapshot of the MD trajectory and found that one of the three Euler angles, ψ , is subject to larger oscillations (see their Gaussian distributions and σ collected in Figure S11) and is therefore more likely to contribute to electron-phonon coupling. Inspection of Figure S12 shows indeed that the ψ angle oscillations with respect to the crystal geometry, for the two monomers forming the D2 dimer, display a good linear correlation with electronic coupling fluctuations and this is even more clear when considering the out of phase combination of the two angles. To further explore the nature of these inter-molecular motions, we determined the frequencies of the lattice vibrations governing electronic-coupling fluctuations, from the Fourier transforms of the autocorrelation function of the *intra-layer* electronic coupling D2 (see Figure 8) and found that they fall in the $15\text{--}80\text{ cm}^{-1}$ region. Inspection of the rigid-body lattice vibrations computed for super-cells of **FNDI** shows a number of modes with frequencies falling in the active region, (see the bottom part of Figure 8) in which pairs of adjacent **FNDI**s (in particular those forming D2 dimers) undergo an out of phase molecular twist, namely a marked molecular reorientation and not simply a molecular translation, in close agreement with the results from the analysis of Euler angles.

Owing to the overall modest role of thermal fluctuations for **FNDI** it can be concluded that the impact of lattice vibrations will be weak except for the D2 coupling. In this latter case we should consider that, because of its large coupling at the crystal geometry, the rate constant for jump D2 is ca. 11.3 ps^{-1} (see Table 3). This implies that frequencies lower than 400 cm^{-1} are slower than the rate of jump. Therefore, the thermalized approach used for instance for some PDI derivatives¹⁹ cannot

be used here. A correct approach to include thermal effects in the charge propagation within the non-adiabatic hopping model would be to run KMC simulations on MD snapshots as described in refs.^{24,46,55} or following the two-step approach of ref.⁵⁴. These extensions, that will be considered in future investigations, are not expected, however, to change the major conclusions of this work.

Conclusions

We have investigated the electron transport properties in the crystal phase of a fluoro-alkyl NDI derivative and compared the results with those of the corresponding experimental study in single crystal devices.

Quantum-chemical calculations show that fluorinated substituents at the imide position enhances the n-type character by lowering the LUMO levels and increasing the computed electronic affinities.

Calculations of charge transfer rate constants, according to the non-adiabatic hopping approach, and propagation of the charge carriers within a KMC scheme, lead to predicted charge mobilities of **FNDI** that compare very well with the experimental measurements in single-crystal devices fabricated with the organic-ribbon mask technique.

The marked anisotropy in the *b,c* plane is nicely reproduced by the calculations and rationalized in terms of the available charge pathways displaying not negligible electronic couplings. More specifically, charge transport is enhanced along the *c* direction by the presence of two pathways (D4 and D5) along this axis to which a contribution from two efficient zig-zag pathways (D1 and D2) also directed along the *c* axis is summed up. In contrast, for charge transport along *b*, a mechanism of dimer trapping is envisaged, similar to what has previously been shown to depress mobility in some core twisted chlorinated PDI derivatives.¹⁹

The effect of thermal motion on the modulation of electronic couplings has been investigated with an integrated classical mechanics / quantum-mechanics approach and it has been shown that while for modest electron-phonon couplings a linear relationship between electronic-coupling fluctuations and molecular distance is obeyed, for the largest electron-phonon couplings characterizing the D2 pathway, also molecular reorientation plays a relevant role. This was confirmed by identifying the frequencies of active lattice vibrations via the Fourier transform of the autocorrelation functions of the electronic couplings and combining this information with the inspection of lattice vibration eigenvectors falling in the active frequency region which is located in the $20\text{--}80\text{ cm}^{-1}$ range.

The study reveals a less relevant role of electronic coupling fluctuations (non-local electron-phonon couplings) compared to PDI derivatives, possibly as a result of the less expanded conjugated core and associated π - π stacking.

On the other hand the close agreement between observed and computed charge transport properties demonstrates the reliability of the model in this case, for the interpretation of data obtained from single crystal devices of **FNDI**.

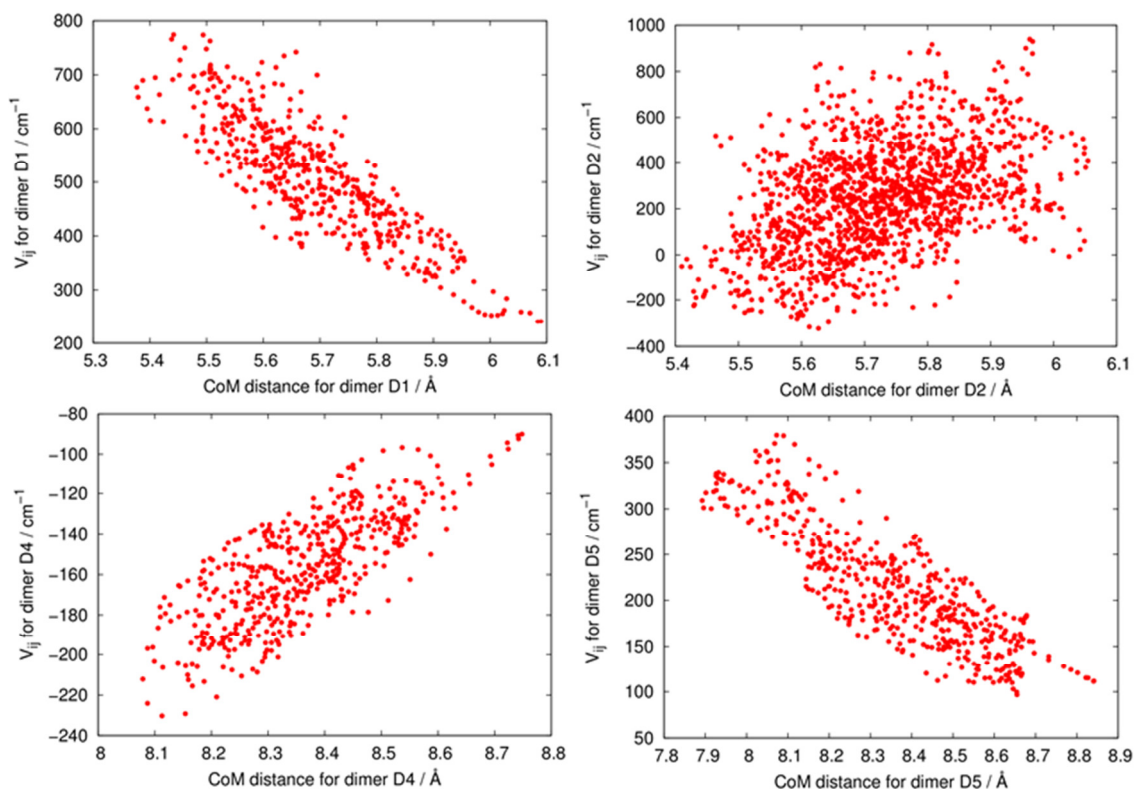


Figure 7. Correlation between CoM distance variations and the electronic coupling V_{ij} associated with dimer D1 (top, left); dimer D2 (top, right); dimer D4 (bottom, left); dimer D5 (bottom, right).

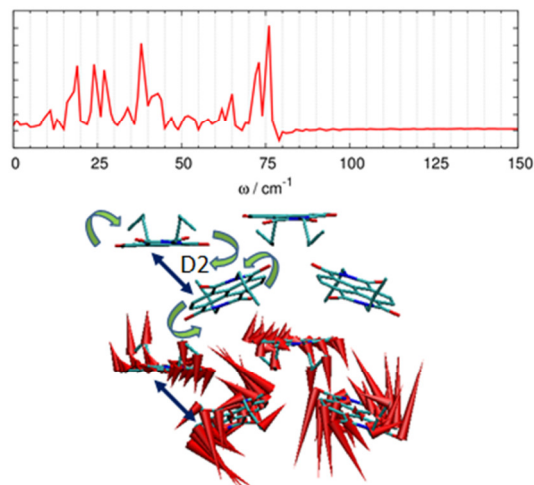


Figure 8. (top) Fourier transform of the autocorrelation function of the computed electronic couplings and, (bottom) graphical representation of one lattice vibrations ($\omega=67 \text{ cm}^{-1}$) governing the modulation of the *intra-layer* coupling D2 (blue arrows) and whose nuclear motion corresponds to reorientation of the two molecules forming the D2 dimer. In the top part of the crystal portion only molecules with a schematic representation of their motion (green arrows) are shown to facilitate the visualization of the nuclear motion (by red cones) in the bottom part.

Notes and references

^a Università di Bologna, Dipartimento di Chimica ‘G. Ciamician’, Via F. Selmi, 2, 40126 Bologna, Italy.

^b INSTM, UdR Bologna, Italy. E-mail: fabrizia.negri@unibo.it

Electronic Supplementary Information (ESI) available: [Details on computational models, seight tables including absolute energies for all the computed structures, frontier molecular orbital energies, intermolecular reorganization energies, computed electron affinities, Huang-Rhys parameters, eigenvalues of the mobility tensor. Additional figures including a schematic representation of electron affinities and reorganization energies, the crystal structure of the systems investigated, the radial distribution functions from MD simulations, the geometry change upon charging for the NDI derivatives investigated, the frontier molecular orbitals, the vibrational contribution to intramolecular reorganization energies, a short KMC trajectory showing dimer-trapping effects, the Gaussian distribution of electronic coupling fluctuations and Euler angles fluctuations.]. See DOI: 10.1039/b000000x/

1. J. E. Anthony, A. Facchetti, M. Heeney, S. R. Marder, and X. Zhan, *Adv. Mater.*, 2010, **22**, 3876–3892.
2. X. Zhan, A. Facchetti, S. Barlow, T. J. Marks, M. A. Ratner, M. R. Wasielewski, and S. R. Marder, *Adv. Mater.*, 2011, **23**, 268–284.
3. F. Würthner and M. Stolte, *Chem. Commun.*, 2011, **47**, 5109.
4. S. V. Bhosale, S. V. Bhosale, and S. K. Bhargava, *Org. Biomol. Chem.*, 2012, **10**, 6455–6468.

5. Y. Li, W. Xu, S. Di Motta, F. Negri, D. Zhu, and Z. Wang, *Chem. Commun.*, 2012, **48**, 8204–8206.
6. W. Yue, A. Lv, J. Gao, W. Jiang, L. Hao, C. Li, Y. Li, L. E. Polander, S. Barlow, W. Hu, S. Di Motta, F. Negri, S. R. Marder, and Z. Wang, *J. Am. Chem. Soc.*, 2012, **134**, 5770–5773.
7. M. Gsanger, J. H. Oh, M. Konemann, W. Hoffken, A. M. Krause, Z. Bao, F. Würthner, *Angew. Chem., Int. Ed. Engl.* 2010, **49**, 740–743.
8. S. Fabiano, H. Wang, C. Piliago, C. Jaye, D. A. Fischer, Z. Chen, B. Pignataro, A. Facchetti, Y.-L. Loo, M. A. Loi, *Adv. Funct. Mater.*, 2011, **21**, 4479–4486.
9. H. Katz, A. Lovinger, J. Johnson, C. Kloc, T. Siegrist, W. Li, Y. Lin, and a. Dodabalapur, *Nature*, 2000, **404**, 478–81.
10. H. E. Katz, J. Johnson, A. J. Lovinger, and W. Li, *J. Am. Chem. Soc.*, 2000, **122**, 7787–7792.
11. D. Shukla, S. F. Nelson, D. C. Freeman, M. Rajeswaran, W. G. Ahearn, D. M. Meyer, and J. T. Carey, *Chem. Mater.*, 2008, **20**, 7486–7491.
12. T. He, M. Stolte, and F. Würthner, *Adv. Mater.*, 2013, **25**, 6951–6955.
13. W.-Y. Lee, J. H. Oh, S.-L. Suraru, W.-C. Chen, F. Würthner, and Z. Bao, *Adv. Funct. Mater.*, 2011, **21**, 4173–4181.
14. J. H. Oh, S.-L. Suraru, W.-Y. Lee, M. Könemann, H. W. Höffken, C. Röger, R. Schmidt, Y. Chung, W.-C. Chen, F. Würthner, and Z. Bao, *Adv. Funct. Mater.*, 2010, **20**, 2148–2156.
15. Y. Geng, S.-X. Wu, H.-B. Li, X.-D. Tang, Y. Wu, Z.-M. Su, and Y. Liao, *J. Mater. Chem.*, 2011, **21**, 15558.
16. A. Lv, Y. Li, W. Yue, L. Jiang, H. Dong, G. Zhao, Q. Meng, W. Jiang, Y. He, Z. Li, Z. Wang, and W. Hu, *Chem. Commun.*, 2012, **48**, 5154.
17. L. Jiang, J. Gao, E. Wang, H. Li, Z. Wang, W. Hu, and L. Jiang, *Adv. Mater.*, 2008, **20**, 2735–2740.
18. E. Di Donato, R. P. Fornari, S. Di Motta, Y. Li, Z. Wang, and F. Negri, *J. Phys. Chem. B*, 2010, **114**, 5327–5334.
19. S. Di Motta, M. Siracusa, and F. Negri, *J. Phys. Chem. C*, 2011, **115**, 20754–20764.
20. S. Di Motta, E. Di Donato, F. Negri, G. Orlandi, D. Fazzi, and C. Castiglioni, *J. Am. Chem. Soc.*, 2009, **131**, 6591–6598.
21. A. Troisi, *Chem. Soc. Rev.*, 2011, **40**, 2347–2358.
22. A. Troisi, *Mol. Simul.*, 2006, **32**, 707–716.
23. A. Troisi and G. Orlandi, *J. Phys. Chem.*, 2006, **110**, 4065–4070.
24. N. G. Martinelli, Y. Olivier, S. Athanasopoulos, M.-C. R. Delgado, K. R. Pigg, D. A. da S. Filho, R. S. Sánchez-Carrera, E. Venuti, R. G. D. Valle, J.-L. Brédas, D. Beljonne, and J. Cornil, *ChemPhysChem*, 2009, **10**, 2265–2273.
25. J.-L. Brédas, D. Beljonne, V. Coropceanu, and J. Cornil, *Chem. Rev.*, 2004, **104**, 4971–5004.
26. V. Coropceanu, J. Cornil, D. A. da Silva Filho, Y. Olivier, R. Silbey, and J.-L. Brédas, *Chem. Rev.*, 2007, **107**, 926–952.
27. M. J. Frisch, G. W. Trucks, H. B. Schlegel, G. E. Scuseria, M. A. Robb, J. R. Cheeseman, G. Scalmani, V. Barone, B. Mennucci, G. A. Petersson, H. Nakatsuji, M. Caricato, X. Li, H. P. Hratchian, A. F. Izmaylov, J. Bloino, G. Zheng, J. L. Sonnenberg, M. Hada, M. Ehara, K. Toyota, R. Fukuda, J. Hasegawa, M. Ishida, T. Nakajima, Y. Honda, O. Kitao, H. Nakai, T. Vreven, J. A. J. Montgomery, J. E. Peralta, F. Ogliaro, M. Bearpark, J. J. Heyd, E. Brothers, K. N. Kudin, V. N. Staroverov, R. Kobayashi, J. Normand, K. Raghavachari, A. Rendell, J. C. Burant, S. S. Iyengar, J. Tomasi, M. Cossi, N. Rega, N. J. Millam, M. Klene, J. E. Knox, J. B. Cross, V. Bakken, C. Adamo, J. Jaramillo, R. Gomperts, R. E. Stratmann, O. Yazyev, A. J. Austin, R. Cammi, C. Pomelli, J. W. Ochterski, R. L. Martin, K. Morokuma, V. G. Zakrzewski, G. A. Voth, P. Salvador, J. J. Dannenberg, S. Dapprich, A. D. Daniels, Ö. Farkas, J. B. Foresman, J. V. Ortiz, J. Cioslowski, and D. J. Fox, Gaussian 09, Revision A.02, 2009.
28. Y. Song, C. Di, X. Yang, S. Li, W. Xu, Y. Liu, L. Yang, Z. Shuai, D. Zhang, and D. Zhu, *J. Am. Chem. Soc.*, 2006, **128**, 15940–15941.
29. D. L. Cheung and A. Troisi, *Phys. Chem. Chem. Phys.*, 2008, **10**, 5941.
30. P. F. Barbara, T. J. Meyer, and M. A. Ratner, *J. Phys. Chem.*, 1996, **100**, 13148–13168.
31. J. Jortner, *J. Chem. Phys.*, 1976, **64**, 4860–4867.
32. R. A. Marcus, *J. Chem. Phys.*, 1956, **24**, 966–978.
33. V. Stehr, B. Engels, C. Deibel, R. F. Fink, *J. Chem. Phys.*, 2014, **140**, 024503.
34. J. Cornil, S. Verlaak, N. Martinelli, A. Mityashin, Y. Olivier, T. V. Regemorter, G. D'Avino, L. Muccioli, C. Zannoni, F. Castet, D. Beljonne, and P. Heremans, *Accounts Chem. Res.*, 2013, **46**, 434–443.
35. D. P. McMahon and A. Troisi, *J. Phys. Chem. Lett.*, 2010, **1**, 941–946.
36. V. Marcon, D. W. Breiby, W. Pisula, J. Dahl, J. Kirkpatrick, S. Patwardhan, F. Grozema, and D. Andrienko, *J. Am. Chem. Soc.*, 2009, **131**, 11426–11432.
37. Y. Olivier, V. Lemaure, J. L. Brédas, and J. Cornil, *J. Phys. Chem.*, 2006, **110**, 6356–6364.
38. G. Nan, X. Yang, L. Wang, Z. Shuai, and Y. Zhao, *Phys. Rev. B*, 2009, **79**.
39. X. Yang, L. Wang, C. Wang, W. Long, and Z. Shuai, *Chem. Mater.*, 2008, **20**, 3205–3211.
40. S. Athanasopoulos, J. Kirkpatrick, D. Martinez, J. M. Frost, C. M. Foden, A. B. Walker, and J. Nelson, *Nano Lett.*, 2007, **7**, 1785–1788.
41. M. J. Sailor and E. C. Wu, *Adv. Funct. Mater.*, 2009, **19**, 3195–3208.
42. L. Tan, L. Zhang, X. Jiang, X. Yang, L. Wang, Z. Wang, L. Li, W. Hu, Z. Shuai, L. Li, and D. Zhu, *Adv. Funct. Mater.*, 2009, **19**, 272–276.
43. D. Andrienko, J. Kirkpatrick, V. Marcon, J. Nelson, and K. Kremer, *Phys. Status solidi*, 2008, **245**, 830–834.
44. M. Schrader, C. Körner, C. Elschner, and D. Andrienko, *J. Mater. Chem.*, 2012, **22**, 22258.
45. X. D. Yang, L. J. Wang, C. L. Wang, W. Long, Z. G. Shuai, *Chem. Mater.* 2008, **20**, 3205–3211.
46. Y. Olivier, L. Muccioli, V. Lemaure, Y. H. Geerts, C. Zannoni, and J. Cornil, *J. Phys. Chem. B*, 2009, **113**, 14102–14111.
47. J. J. Kwiatkowski, J. Nelson, H. Li, J. L. Bredas, W. Wenzel, and C. Lennartz, *Phys. Chem. Chem. Phys.*, 2008, **10**, 1852–1858.
48. N. L. Allinger, H. Y. Yuh, J. H. Lii, *J. Am. Chem. Soc.*, 1989, **111**, 8551–8566.
49. TINKER, Software Tools for Molecular Design version 5.1 (2009).
50. H. J. C. Berendsen, J. P. M. Postma, W. F. van Gusteren, A. Di Nola, J. R. Haak, *J. Chem. Phys.*, 1984, **81**, 3684–3690.

51. D. Fazzi, C. Castiglioni, and F. Negri, *Phys. Chem. Chem. Phys.*, 2010, **12**, 1600–1609.
52. W.-Q. Deng and W. A. Goddard, *J. Phys. Chem. B*, 2004, **108**, 8614–8621.
53. V. Stehr, J. Pfister, R. F. Fink, B. Engels, C. Deibel, *Phys. Rev. B*, 2011, **83**, 155208.
54. Z. Shuai, H. Geng, W. Xu, Y. Liao, and J.-M. André, *Chem. Soc. Rev.*, 2014, **43**, 2662.
55. J. Nelson, J. J. Kwiatkowski, J. Kirkpatrick, and J. M. Frost, *Accounts Chem. Res.*, 2009, **42**, 1768–1778.